








Optimization of the efficiency of a nanowire solar cell by nanowire tapering

Cite as: J. Appl. Phys. **134**, 223104 (2023); doi: [10.1063/5.0176935](https://doi.org/10.1063/5.0176935)

Submitted: 18 September 2023 · Accepted: 21 November 2023 ·

Published Online: 11 December 2023



Emanuele Bochicchio,  Ksenia Korzun,  Friso Dubach,  Bas T. van Gorkom, Roel J. Theeuwes,  Wilhelmus M. M. (Erwin) Kessels,  Jaime Gómez Rivas,  and Jos E. M. Haverkort^{a)} 

AFFILIATIONS

Department of Applied Physics, Eindhoven University of Technology, De Groene Loper 19, Eindhoven, The Netherlands

^{a)}Author to whom correspondence should be addressed: j.e.m.haverkort@tue.nl

ABSTRACT

Thermodynamics shows that the open-circuit voltage (V_{oc}) of a solar cell is dependent on the external radiative efficiency at V_{oc} . In planar solar cells with low photon recycling probability, this efficiency is limited to 2% due to total internal reflection of the emitted light, providing a penalty of 101 mV to the V_{oc} . Tapered nanowire solar cells allow for an adiabatic expansion of the guided optical mode into air, allowing to reduce this loss. For this purpose, we first perform simulations of the photon escape probability in tapered nanowires with both finite difference time domain simulations as well as with rigorous coupled-wave analysis, showing photon escape probabilities up to 47.2% for normally tapered nanowires and up to 92% for inversely tapered nanowires. We subsequently show that by fine tuning the recipe for reactive ion etching of the tapered InP nanowires, we can decrease the nanowire tapering angle from 4.5° down to 1.8° , allowing to significantly increase the measured external radiative efficiency. We finally observe an open-circuit voltage of 0.746 V at a tapering angle of 2.46° .

© 2023 Author(s). All article content, except where otherwise noted, is licensed under a Creative Commons Attribution (CC BY) license (<http://creativecommons.org/licenses/by/4.0/>). <https://doi.org/10.1063/5.0176935>

16 December 2023 09:09:16

I. INTRODUCTION

For the optimization of a solar cell, the most obvious route is to optimize the solar light absorption as well as the current conversion efficiency by, e.g., reducing carrier losses due to nonradiative recombination. This commonly chosen approach mainly optimizes the short-circuit current while leaving the open-circuit voltage untouched. The optimization of the open-circuit voltage requires a thermodynamic approach in which the external radiative emission rate should be made equal to the impinging solar radiation rate on the solar cell in order to arrive at the radiative limit^{1–4} for the open-circuit voltage, which is also called the detailed balance limit. This requirement is easy to understand since a solar photon that is absorbed in a lossless solar cell at open-circuit condition ($I = 0$) has no other option than leaving the cell again as a photon. Any other option either creates a loss or generates an external current, which is not possible at open-circuit. For a realistic solar cell which is not lossless, this implies that the external radiative efficiency should be maximized to optimize the open-circuit voltage and to approach the radiative limit of the solar cell, which is explained by the

following formula:^{1,4,5}

$$V_{oc} = V_{oc}^{rad} - \left| \frac{kT}{q} \ln(\eta_{ext}^{PL}) \right|. \quad (1)$$

For a realistic semiconductor with a low internal radiative efficiency η_{int} , the external radiative efficiency η_{ext} is simply the product of the internal radiative efficiency and the photon escape probability $\overline{P_{esc}}$ averaged over all emission angles of the photon as given by

$$\eta_{ext}^{PL} = \eta_{int} \overline{P_{esc}}. \quad (2)$$

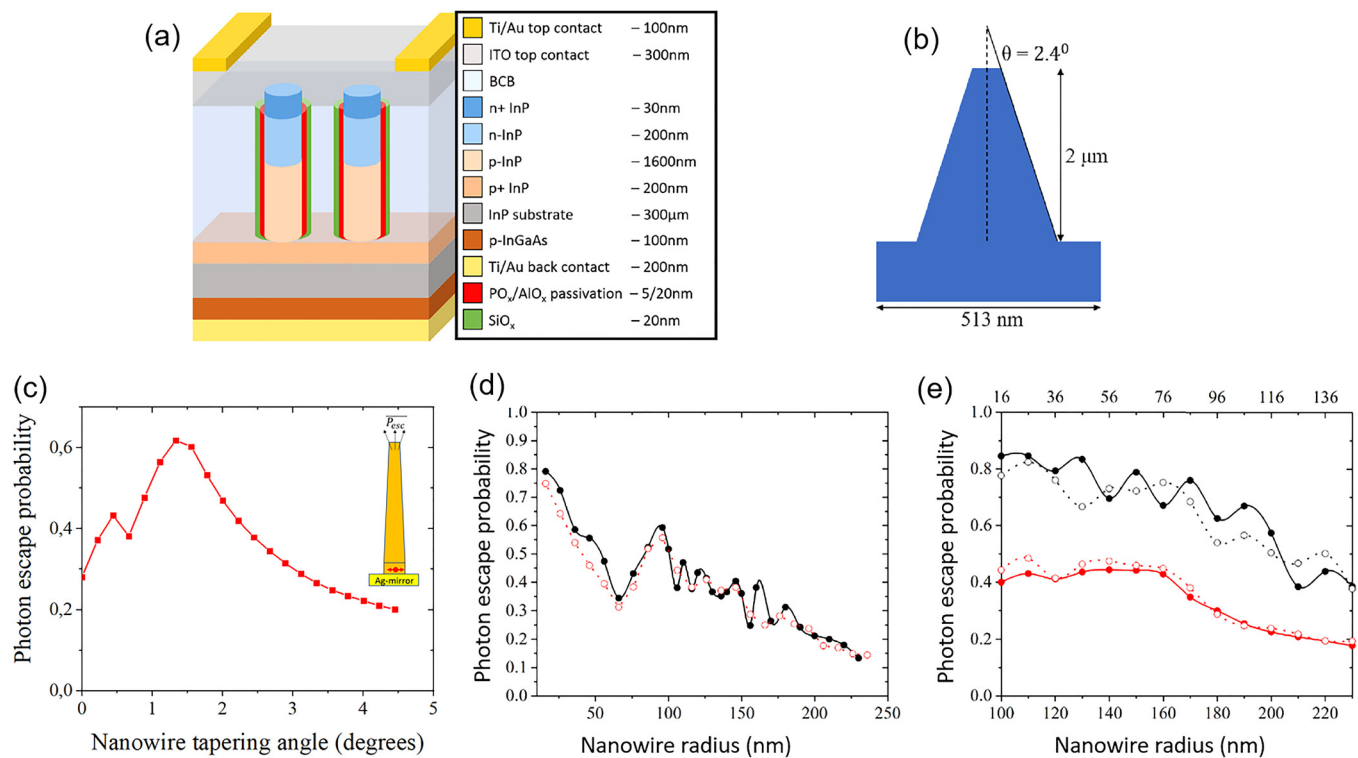
It is important to understand that Eq. (1) contains the photon escape probability since any photon that is not capable to leave the cell, e.g., by total internal reflection, will be re-absorbed and be lost due to subsequent nonradiative recombination. As an example, for $\eta_{int} \ll 1$ and $\overline{P_{esc}} = 2\%$, 98% of the light that would be externally emitted by a cell with $\overline{P_{esc}} = 100\%$ is now lost by nonradiative

recombination. This shows that one has to optimize the photon escape probability to limit the nonradiative loss and, thus, to optimize V_{oc} . Unfortunately, the additive terms in Eq. (1) are in general not completely independent for nanostructures,^{1,6,7} implying that V_{oc}^{rad} is generally not a constant. We will, however, show in Sec. 1 in the [supplementary material](#) that V_{oc}^{rad} is identical for a conically tapered nanowire as treated in this paper and a thick planar solar cell.

The photon escape probability at the front surface⁸ of a planar InP cell can be approximated as $\overline{P_{esc}} = \frac{1}{4n^2} = 2\%$, which is determined by the total internal reflection of all photons impinging from the inside of the solar cell at the front surface. Most photons are totally internally reflected, while only a small number of photons hit the front surface inside of a small emission cone allowing them to escape the cell and to contribute to the external radiative efficiency. It has been mostly overlooked that the small photon escape probability in a planar cell with low η_{int} provides an additional V_{oc} -penalty as large as 101 mV at room temperature (300 K) according to Eq. (1). This V_{oc} -penalty can only be eliminated⁹ in extremely high quantum efficiency materials in which photon recycling allows multiple photon recycling events to redirect all emitted

photons into the small emission cone of the material in which total internal reflection is absent.

A semiconductor nanowire solar cell as shown in Fig. 1(a) imposes a fundamental improvement for the photon escape probability since properly tapered nanowires allow all light emitted into the guided HE_{11} -mode to adiabatically expand into the surrounding air. For a dipole located at the bottom of a single nanowire [as shown in the inset of Fig. 1(c)], it has previously been shown¹⁰ that the photon escape probability through the top facet amounts to 62%, showing that an appreciable fraction of the light leaves the nanowire through the side facets. Since the emission from the side facets is partially re-absorbed into neighboring nanowires and subsequently re-emitted through the top facet of such a neighboring nanowire, it is of importance to calculate the photon escape probability of the complete nanowire array. Such a calculation will be performed in Sec. II, where we will optimize the shape of the tapered nanowire by both finite difference time domain (FDTD) and rigorous coupled-wave analysis (RCWA) simulations. In Sec. III, we employ a particle swarm optimization procedure and show that an array of inversely tapered nanowires features a photon escape probability of 92%, thus allowing to almost completely



16 December 2023 09:09:16

FIG. 1. (a) Schematic overview of a nanowire solar cell with respective layer thicknesses which will be further discussed in Sec. VI. (b) Detailed nanowire geometry with a tapering angle of 2.4° , a height of $2\mu m$, and a pitch of 513 nm . (c) Photon escape probability from the top facet of a nanowire with a height of $2\mu m$ on a silver mirror, as a function of the tapering angle for a single dipole emitter positioned in the middle of the bottom straight part with a height of 200 nm and a bottom radius of 120 nm . (d) Photon escape probability from the top facet of a nanowire array on InP without tapering as a function of radius, calculated using RCWA (black curve) and FDTD (red curve). (e) Photon escape probability from the top facet of normally tapered (red curves) and inversely tapered (black curves) nanowire arrays on InP as a function of the large radius (bottom axis) and the small radius (top axis), calculated using RCWA (solid lines) and FDTD (dashed lines).

eliminate the related V_{oc} -loss. In Sec. IV, we will focus on the fabrication of tapered nanowires by reactive ion etching, showing that we are able to reduce the tapering angle down to 1.8° for normally tapered wires. This implies that a significant reduction of the V_{oc} -loss is experimentally within reach. Section V is focused to the influence of the tapering angle on the photon escape probability. We show a clear increase of the external radiative efficiency for lower tapering. Finally in Sec. VI, we report tapered nanowire solar cells with tapering angles of both 2.8° and 2.4° , showing that the 2.4° tapered nanowire solar cell features a solar cell efficiency up to 17.8%. More importantly, we are able to show that the 2.4° tapered nanowire solar cells show improved open-circuit voltage as compared to their 2.8° counterparts, thus providing the first experimental evidence that the open-circuit voltage is indeed dependent of the photon escape probability.

II. SIMULATION OF THE PHOTON ESCAPE PROBABILITY FOR TAPERED NANOWIRE ARRAYS

We have chosen a tapered nanowire array with a nanowire height of $2\mu\text{m}$, a pitch of 513 nm, and a tapering angle $\theta = 2.4^\circ$ [Fig. 1(b)] in order to maximize the solar light absorption.^{11,12} A tapering angle $\theta = 2.4^\circ$ is achieved in our tapered nanowire solar cell as presented in Sec. VI. A cross section of the nanowire solar cell is presented in Fig. 1(a) in order to provide an overview of the complete cell design.

One of the major advantages of nanowire solar cells is the efficient solar light absorption. One can understand this efficient light absorption by the overlap of the absorption cross sections of neighboring nanowires. In addition, the light reflection at the small nanowire tip of a tapered nanowire is very weak due to the low effective refractive index of the top layer of a tapered nanowire array.¹³ Anttu *et al.*¹¹ have simulated the solar light absorption in an array of cylindrical nanowires and obtained an optimum pitch of 400 nm for which 94% of the light above the bandgap is absorbed by $2\mu\text{m}$ long nanowires. Diedenhofen *et al.*¹² even obtained 98% integrated absorption for $3\mu\text{m}$ long tapered nanowires with a pitch of 513 nm. Due to the reciprocity theorem of light, the large light absorption probability in tapered nanowires has the same physical origin as the large photon escape probability which will be treated in this paper.

The photon escape probability (\overline{P}_{esc}) has previously been optimized¹⁰ for a single dipole emitter positioned in a single nanowire with a silver bottom mirror and with a bottom straight section with a height of $0.2\mu\text{m}$ and a top tapered section with a height of $1.8\mu\text{m}$. For optimizing the tapering, the dipole emitter was positioned in the center of the bottom section. The results of this optimization effort are reproduced in Fig. 1(c). We observe a maximum photon escape probability through the top facet of 62% for a tapering angle of 1.2° – 1.3° . We emphasize that this is not the relevant photon emission probability for a nanowire solar cell since we positioned the emitting dipole at a fixed position at the bottom of the nanowire and we neglected photon recycling of photons emitted from the side facet and being re-absorbed in a neighboring nanowire. In order to calculate the photon escape probability for an arrayed nanowire solar cell, we cannot use the simple point dipole approach¹⁰ together with periodic boundary conditions

since the point dipoles located in one semiconductor nanowire will be periodically repeated in all other nanowires, giving rise to unwanted coherent effects.

In order to obtain quantitative values for the photon escape probability, we have to calculate the incoherent spontaneous emission from the nanowire array. This calculation can be done by implementing the Lorentz reciprocity theorem. This theorem states that the relationship between the local oscillating current (oscillating point dipole) and the electric field it produces will stay unchanged if we swap the position where the oscillating current is located and the position where the electric field is measured. In other words, the radiation of a dipole in the structure in a certain emission direction can be determined from the near field that is calculated after exciting the structure with a plane wave incident from that same direction. To determine the photon escape probability, it is, thus, necessary to calculate the near field by illuminating the sample from all possible directions in the escaping medium. Lorentz reciprocity is valid for linear, dispersive, inhomogeneous, and anisotropic media. It has been successfully applied for the determination of the light extraction from structured LEDs.¹⁴ Simulations based on the reciprocity principle can only quantify the outcoupling of a source to free space, thus the escape probability. Emission into evanescent or dark modes are not considered by reciprocity since incident plane waves from free space cannot couple to these modes.^{15,16}

From the modeling point of view, Lorentz reciprocity implies that we can calculate the emission in the direction opposite to the incident wave by solving the scattering problem for the incident wave. The emitted power into a small angle $d\Omega$ can be expressed as

$$dP_{top(bot)}(\vec{r}, \lambda, \theta_{top(bot)}, \varphi_{top(bot)}) = \hbar \frac{2\pi c}{\lambda} |\vec{p}(\vec{r}, \lambda)| n_{top(bot)}(\lambda) \times E_{enh,top(bot)}^2(\vec{r}, \lambda, \theta_{top(bot)}, \varphi_{top(bot)}) d\lambda dV d\Omega, \quad (3)$$

where θ and φ are the polar and azimuthal angles of emitted light, $\vec{p}(\vec{r}, \lambda)$ is the dipole moment density which is assumed to be isotropically distributed, and $n_{top(bot)}$ is the refractive index of the medium around the nanowire for the top and bottom(bot) hemispheres, respectively. The emitted power $dP_{top(bot)}$ should first be calculated separately for both the TE and TM polarization of the incident plane wave, adding both contributions later in Eq. (5). The local field enhancement at the dipole location \vec{r} is equal to

$$E_{enh,top(bot)}^2(\vec{r}, \lambda, \theta_{top(bot)}, \varphi_{top(bot)}) = \frac{|E_{loc,top(bot)}(\vec{r}, \lambda, \theta_{top(bot)}, \varphi_{top(bot)})|^2}{|E_{in,top(bot)}(\vec{r}, \lambda, \theta_{top(bot)}, \varphi_{top(bot)})|^2}, \quad (4)$$

where $E_{in,top(bot)}(\vec{r}, \lambda, \theta_{top(bot)}, \varphi_{top(bot)})$ corresponds to the electric field of the incoming plane wave. We subsequently calculate the total power emitted to the top and to the bottom hemispheres from a nanowire, normalized to the power emitted in a homogeneous environment with a refractive index of the bulk material n_{Bulk} . This

is given by

$$P(\vec{r}, \lambda, \theta, \varphi) = \frac{1}{V_{NW} P_{n_{bulk}}} \int_{V_{NW}} \int_0^{2\pi} d\varphi \int_0^{\pi/2} d\theta \times [dP_{TE}(\vec{r}, \lambda, \theta, \varphi) + dP_{TM}(\vec{r}, \lambda, \theta, \varphi)] \sin\theta d\theta dV, \quad (5)$$

where we have dropped the *top(bot)* subscripts to improve readability. From this equation, the photon escape probability to the top hemisphere of a lossless nanowire can easily be calculated by

$$\overline{P_{esc}} = \frac{P_{top}}{P_{top} + P_{bot}}. \quad (6)$$

The calculation of the local field enhancement is time consuming. We can, however, express the integrated field enhancement over the nanowire volume in terms of the absorption inside the nanowire,¹⁷

$$\int_{V_{NW}} E_{enh,top(bot)}^2(\vec{r}, \lambda, \theta, \varphi) dV = \frac{A_{TE(TM)top(bot)}(\vec{r}, \lambda, \theta, \varphi) n_{top(bot)}(\lambda) p^2 \cos\theta}{\frac{4\pi}{\lambda} \text{Re}(n_{NW}) \text{Im}(n_{NW})}, \quad (7)$$

where $A_{TE(TM)top(bot)}(\vec{r}, \lambda, \theta, \varphi)$ is the light absorption for *TE(TM)* polarized light emerging either from the air (top) or from the substrate (bot) hemisphere, p is the period of the nanowire array, and n_{NW} is the complex refractive index of the nanowire.

To calculate the photon escape probability ($\overline{P_{esc}}$) by using Lorentz reciprocity, our task is, thus, to calculate the light absorption of a nanowire by an incident plane wave with a wavelength equal to the emission wavelength of InP, which is 920 nm. For this purpose, we, thus, have to calculate the light transmission and reflection for every incident angle for light approaching the nanowire from both the top and the bottom interfaces of the array. This task is performed by Finite Difference Time Domain (FDTD) calculations in the Lumerical software package. For practical purposes, the incident angle of the plane wave is varied from 0° to 88°. The refractive index of substrate is set to $n_{sub} = 3.41$, whereas we add a small imaginary part of 10^{-4} to the refractive index of the nanowire ($n_{NW} = 3.41 + 10^{-4}i$) in order to be able to calculate the electric field enhancement from the amount of light absorption by using Eq. (7). For calculating $\overline{P_{esc}}$, we, thus, include re-absorption of emitted photoluminescence.

In order to check the computational accuracy of our FDTD method and to be able to optimize the amount of tapering for the highest photon escape probability in Sec. III, we also calculate $\overline{P_{esc}}$ using the rigorous coupled-wave analysis (RCWA) method, which is a Fourier-space method for solving Maxwell's equations in the frequency domain.¹⁸ The main advantage of the RCWA method is that it is numerical only in two dimensions and analytical in the third dimension, as shown in Sec. 2 in the [supplementary material](#). To model the behavior of tapered nanowires, the structure is divided into multiple (around 25) layers with a cylinder of a certain radius in every layer, therefore creating a tapered structure. This

simulation is more time consuming than for straight nanowires because of increased number of layers. Moreover, this technique is used to perform an optimization of a nanowire array geometry toward the highest photon escape probability in Sec. III.

In order to choose the number of in-plane Fourier orders in the RCWA calculation, we compare the calculated values of $\overline{P_{esc}}$ obtained with the RCWA method with those of the FDTD technique. We obtain the best correspondence between the two techniques when we use 50 harmonics in the RCWA method. Figure 1(d) shows $\overline{P_{esc}}$ calculated for cylindrical nanowires without tapering as a function of radius using RCWA (black curve) and FDTD (red curve). For small radii, the high outcoupling efficiency is caused by the fact that emission within the nanowire is mostly coupled to leaky modes, whereas for larger radii and better confinement of the modes, $\overline{P_{esc}}$ drastically decreases. Figure 1(e) shows $\overline{P_{esc}}$ for normally tapered (red curves, $r_{bottom} > r_{top}$) and inversely tapered (black curves, $r_{bottom} < r_{top}$) nanowires as a function of the large radius (bottom axis) with solid curves for the RCWA calculation and dashed curves for the FDTD method. The top axis corresponds to the small radius (top axis), which has been calculated from the bottom radius and the tapering angle.

In general, a low photon escape probability from the top facet of a nanowire with high enough radius (>100 nm) on a native substrate can be explained by the fact that due to the low difference between the refractive indices of the nanowire and substrate there is almost no reflection from the substrate and, therefore, a substantial part of the emitted light is lost into the substrate. In Fig. 1(d), as well as for inversely tapered wires, we still obtain a photon escape probability above 50% since the effective refractive indices of the modes existing within the nanowire with small radius are much lower than the refractive index of a bulk material (InP in our case), thus increasing the amount of reflection of the emitted light at the nanowire–substrate interface.

For normally tapered nanowires, we find an optimum photon escape efficiency of 44.6% with the RCWA technique and of 47.2% with the FDTD method as shown in Fig. 1(e). $\overline{P_{esc}}$ is always higher for inversely tapered nanowires than for a normally tapered nanowires. This result is partly counterintuitive since we expect a strong backreflection at the top facet of the inversely tapered nanowire. For the small bottom radii, the effective refractive indices of the leaky modes propagating within the nanowire are much lower than the refractive index of a bulk substrate material (InP in our case). As a consequence, the reflection of leaky modes propagating downward toward the substrate increases. Moreover, for inversely tapered nanowires, the emission reflected from the top facet can be outcoupled from the side facets and reflected back from the substrate leading to a larger $\overline{P_{esc}}$ to the top hemisphere.

III. PARTICLE SWARM OPTIMIZATION OF THE NANOWIRE GEOMETRY

Unfortunately, the photon outcoupling efficiency from the $\theta = 2.4^\circ$ tapered nanowire array as shown in Fig. 1(c) is almost the same as for the nanowires without tapering. This is due to the fact that the relatively large tapering angle of $\theta = 2.4^\circ$ does not allow for a completely lossless adiabatic expansion of the guided mode into the surrounding air. In Sec. II, we discussed how to increase

16 December 2023 09:09:16

$\overline{P_{esc}}$ by fixing the tapering angle to the value obtained in our nanowire solar cell presented in Sec. VI and varying one of the nanowire radii within certain boundaries. Here, we perform a nanowire array geometry optimization using the RCWA technique together with the particle swarm optimization (PSO) algorithm, which is explained in Sec. 3 in the [supplementary material](#).

In this calculation, the distance between neighboring nanowires was fixed to 513 nm. The top and bottom radii were independently varied from 50 to 230 nm and the nanowire length was varied from 1.5 to 2 μm . The higher boundary is restricted by the pitch of 513 nm. The choice of the nanowire length is explained by the interplay between a sufficiently large light absorption and a maximum nanowire length limited by the minority carrier diffusion length. The fitness function chosen for the optimization is $\overline{P_{esc}}$. The optimization is performed for a bandgap wavelength of 920 nm and an incident plane wave with a fixed azimuthal angle of 0° and varying polar angle from 0° to 88° . The number of generations is chosen to be 100 and for every generation there is a set of 20 particles. In the first generation, every particle is assigned with a set of geometrical parameters randomly chosen in between the boundaries described above. The particle swarm optimization leads every particle toward a single set of parameters for which the fitness function ($\overline{P_{esc}}$) is maximized.

Figure 2(a) shows $\overline{P_{esc}}$ as a function of both population number and generation number. The best overall value of $\overline{P_{esc}}$ is equal to 92%, which is gradually reached by almost all particles through the optimization procedure represented in Fig. 2(b). The best value at every generation is represented by black dots, whereas the average value for all the particles in each generation is shown by the red dots. The average value approaches the best value for higher generations, thus proving the validity of the optimization procedure. The plots in Figs. 2(c)–2(e) show the optimization of the nanowire length, the nanowire top radius, and the nanowire bottom radius, respectively, as a function of the generation number. The black dots represent the best values in every generation, and the red dots are the average values over the population in every generation. The best values for the geometric parameters correspond to the best value of $\overline{P_{esc}}$ and are equal to a nanowire height of 1.66 μm , a nanowire bottom radius of 50 nm, and a nanowire top radius of 174 nm. The optimized radii correspond to an inversely tapered nanowire with a tapering angle of 2.1° .

We conclude that the open-circuit voltage penalty, which is 101 mV for a planar cell without efficient photon recycling, reduces to a V_{oc} -penalty of 20.7 mV for a normally tapered nanowire solar cell with an optimum $\overline{P_{esc}} = 45\%$, as seen from the average results of the FDTD and RCWA calculations presented in Fig. 1(d). The

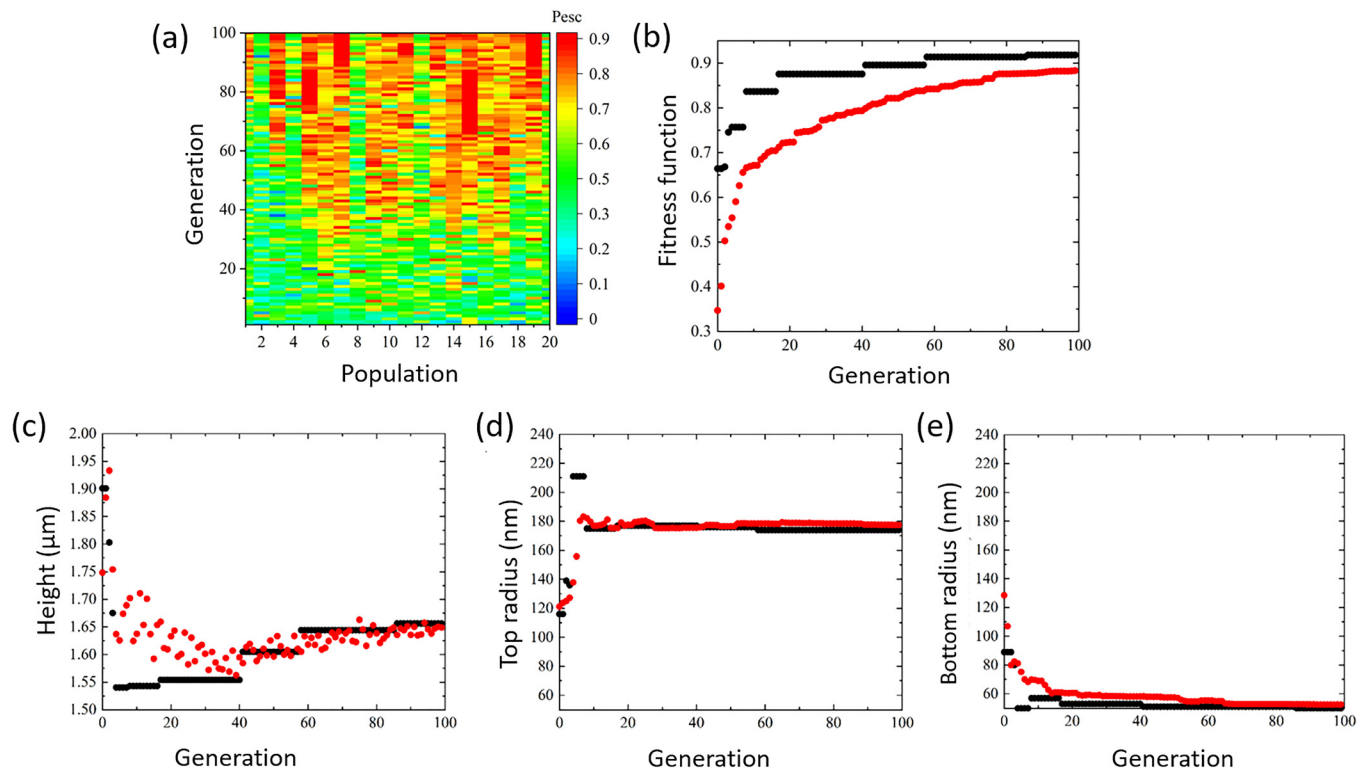


FIG. 2. (a) $\overline{P_{esc}}$ as a function of population and generation. (b) Best value for the fitness function ($\overline{P_{esc}}$) and average values over the population for every generation represented in black and red dots, respectively; best value (black dots) and average value over the population (red dots) for (c) the height, (d) the top radius, and (e) the bottom radius as a function of generation.

TABLE I. Sentech ICP.

	Standard recipe	Optimized recipe
Pressure	6 mTorr	6 mTorr
Temperature	60 °C	60 °C
ICP power	100 W	110 W
Length etching cycle	60 s	50 s
Length descum cycle	15 s	45 s
CH ₄ /H ₂ flow rates	30/70 SCCM	40/60 SCCM

particle swarm optimization of the nanowire tapering further reduces the V_{oc} -penalty to 2.1 mV for an inversely tapered nanowire solar cell with an optimum photon escape probability of $\overline{P_{esc}} = 92\%$ as presented in Fig. 2(b).

IV. FABRICATION OF TAPERED NANOWIRE ARRAYS WITH LOW TAPERING ANGLE

We etch the tapered nanowire array in a Sentech inductively coupled plasma reactor which employs a process of alternating methane–hydrogen chemistry with oxygen cleaning (descum) cycles. The process parameters are presented in Table I. A scanning electron microscopy image of a cross section of a sample etched using the standard recipe can be seen in Fig. 3(a), displaying a tapering profile that appears to feature an almost straight upper section, while the tapering angle gradually gets larger when approaching the bottom of the nanowire. This base-tapered profile, which is a result of the micro-loading effect, is also observed in deep-silicon etching and, more generally, in high-aspect ratio etching.^{19,20} In high-aspect ratio etching, it is more difficult for the radicals to diffuse toward the bottom of the etched features, which

can lead to a relative depletion of radicals near the bottom of the holes, locally resulting in a larger tapering.²⁰

As shown in Fig. 1(c), the optimal shape for the nanowire is a conical tapering, with a tapering angle of 1.2° – 1.3° . The main parameters that influence the etching behavior are (i) the amount of polymer deposition at the nanowire sidewalls, (ii) the plasma chemistry, as governed by the methane and hydrogen flows, and (iii) the temperature of the substrate. Parameters which only marginally influence the tapering angle are the pressure inside the chamber, the plasma density, and the ion directivity toward the substrate, as governed by the Ion Angular Distribution Function (IADF). Mask erosion is also a well-known mechanism for creating a tapering profile, but we did not observe significant mask erosion in our experiments.

The etching and descum cycle lengths were the initial parameters investigated because polymers continuously accumulate during etching, leading to surface passivation. The amount of polymer buildup is highest toward the end of the etching process, which could either increase surface passivation or cause shadowing effects that increase tapering. To achieve the ideal situation to prevent shadowing effects, polymer deposition should occur only in a thin layer around the vertical nanowire sidewalls and not in the etched trenches.

We find that a 50% reduction of the etching cycle length as compared to the standard recipe results in a completely conical tapering profile as shown in Fig. 3(b), indicating that the standard base-tapered profile is partially caused toward the end of the etching process. The improvement of the etched profile comes at the cost of a lower etch rate (from 44.7 down to 40.52 nm/min). The nanowire tapering angle of the upper part of the nanowire also increased to 3.58° (1864 nm tall) for the conical tapering profile.

The relative flow rate of a surface-passivating gas has been used to control the tapering angle in other etching processes.^{21,22} In this study, the relative methane and hydrogen flows were varied

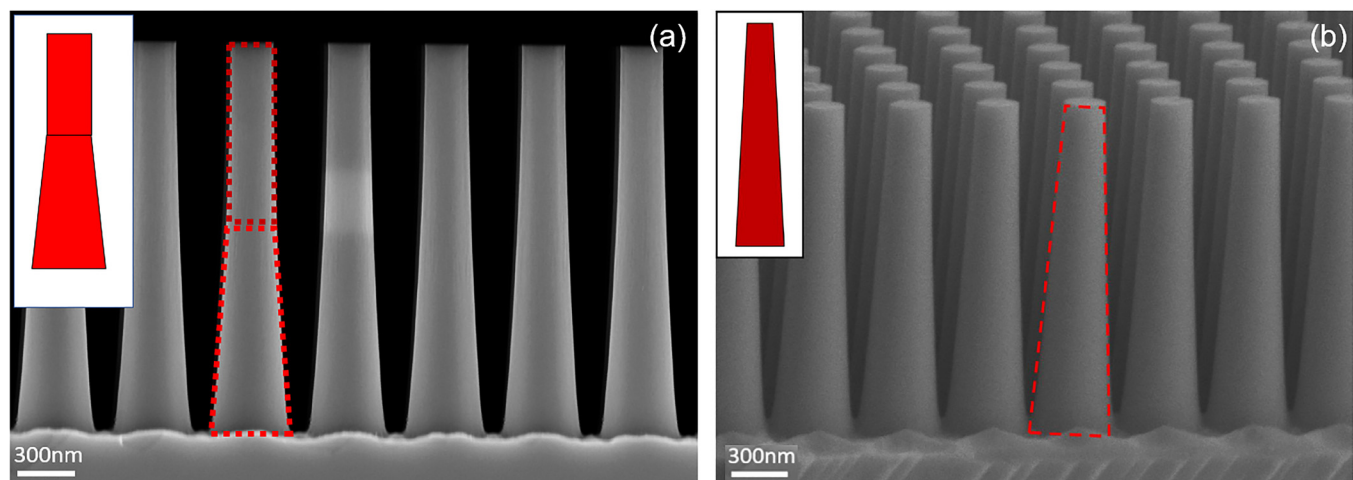


FIG. 3. (a) Scanning electron microscopy (SEM) image of a tapered nanowire array etched with the standard recipe. The nanowires have a pitch of 513 nm and a height of 2056 nm and show increased tapering of 3.5° toward the bottom of the nanowires. (b) SEM image of the conically etched nanowires.

while keeping the total flow rate constant to maintain a constant residence time. Increasing the methane flow from 30 to 35 SCCM resulted in a decreased tapering angle from 4.5° to 3.8° (not shown). We were able to further reduce the tapering angle by increasing the methane flow from 35 to 40 SCCM as shown in Fig. 4(a), showing a clear trend. The nanowires were also slightly taller, and the increased etch rate is consistent with previous studies, which show that InP etching with CH_4/H_2 chemistries is typically limited by etching of indium.^{23–25}

There are several possible mechanisms that could explain the decrease in tapering caused by an increased methane flow rate. One possible reason is that the increased flow rate leads to better surface passivation due to saturation of CH_3 radicals on the inert sidewall surfaces. This will slow down horizontal etching and improve the verticality of the profile, while also enhancing the chemical etching of indium. However, the formation of polymers at the bottom of the trenches can limit the increase in the etch rate. Despite the seemingly opposite effects of these mechanisms, an increase in methane concentration still results in higher chemical etching rates on ion-bombarded bottom surfaces, where polymer formation is inhibited, leading to a more RIE-like profile. On vertical sidewalls that are not exposed to the ion bombardment, polymer deposition will provide effective passivation, resulting in slower etch rates for the vertical sidewalls.

When the methane flow rate increases above a certain point, the methane radicals are not depleted quickly enough through the etching of In, leading to the deposition of polymer films in the trenches in between the wires. This can significantly slow down etching at the bottom of the trenches, especially if the polymer layer is not adequately removed in the descum step. An example of this can be seen in Fig. 4(b), where the etch rate at an increased

methane flow rate is much lower inside the array than outside the array. Polymer buildup will always be present during the etching cycles, but it will become particularly important once the methane flow exceeds the point of CH_3 radical saturation. At this point, the deposition of polymers sharply increases, leading to an early slow-down of etching. Therefore, it is crucial to balance the amount of CH_3 radical saturation by regularly cleaning the polymer buildup for this etching chemistry.

The polymer buildup within the trenches can also be reduced by increasing the amount of ion bombardment by using a higher RF-power. This will leave the amount of polymer formation on the sidewalls unchanged.^{26,27} For this purpose, we increased the RF-power from 100 to 105 W, while using a high methane flow rate with a methane/hydrogen ratio of 40/60 SCCM. The resulting wires are tall and the etch rate is not significantly lower than for other samples, being 40 nm/min. To improve polymer cleaning, the descum cycle length can be increased while decreasing the pressure to allow for a longer diffusion length of the reactive species toward the bottom of the nanowire trenches. This is particularly useful toward the end of the etching procedure when the wires are tall. Although a larger RF-power generally increases the etch rate, it does not significantly affect the tapering profile. This confirms our previous assertion that the main cause of tapering is chemical etching and surface passivation provided by methane radicals.

It is difficult to determine the exact improvements established by varying etching parameters, because we consistently observe a lower tapering angle for increasing etch depth, as shown in Fig. 5(a). This trend is not solely due to increased nanowire length, but also due to the decreasing difference between top and bottom diameters, as shown in Fig. 5(b). For this reason, it is difficult to properly analyze the effect of different etching recipes with the

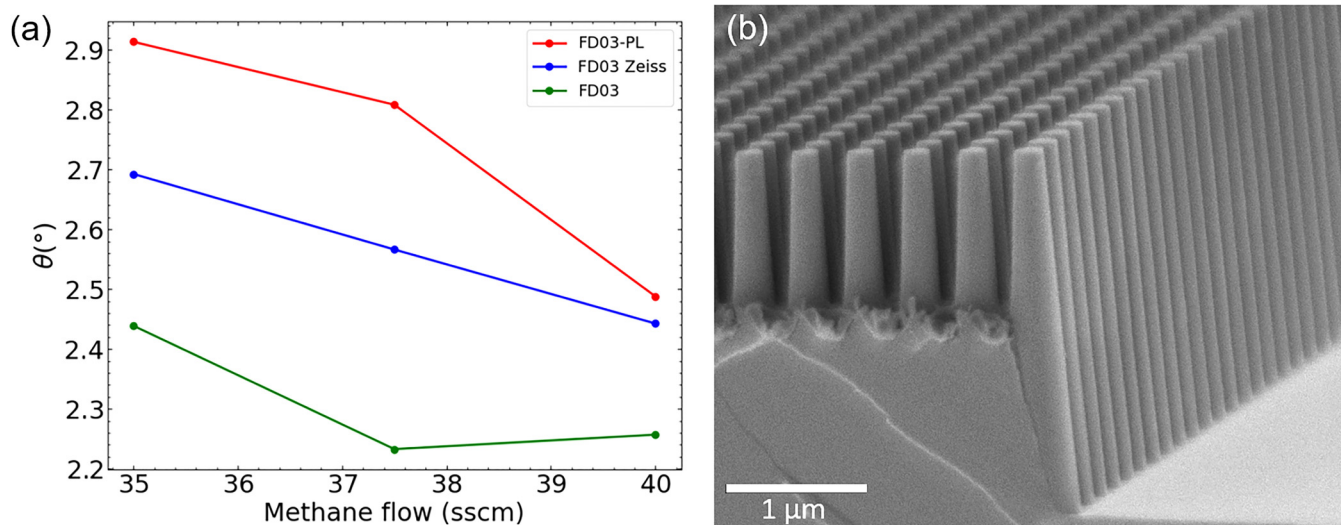


FIG. 4. (a) Optimization of the tapering angle by varying the methane flow, showing a lower tapering at a higher CH_4 flow for samples 7, 9, and 11 of wafer FD03 (see Sec. 4 in the [supplementary material](#) for details). (b) Scanning electron microscopy image showing a strongly reduced etch rate in between the nanowires due to polymer buildup.

16 December 2023 09:09:16

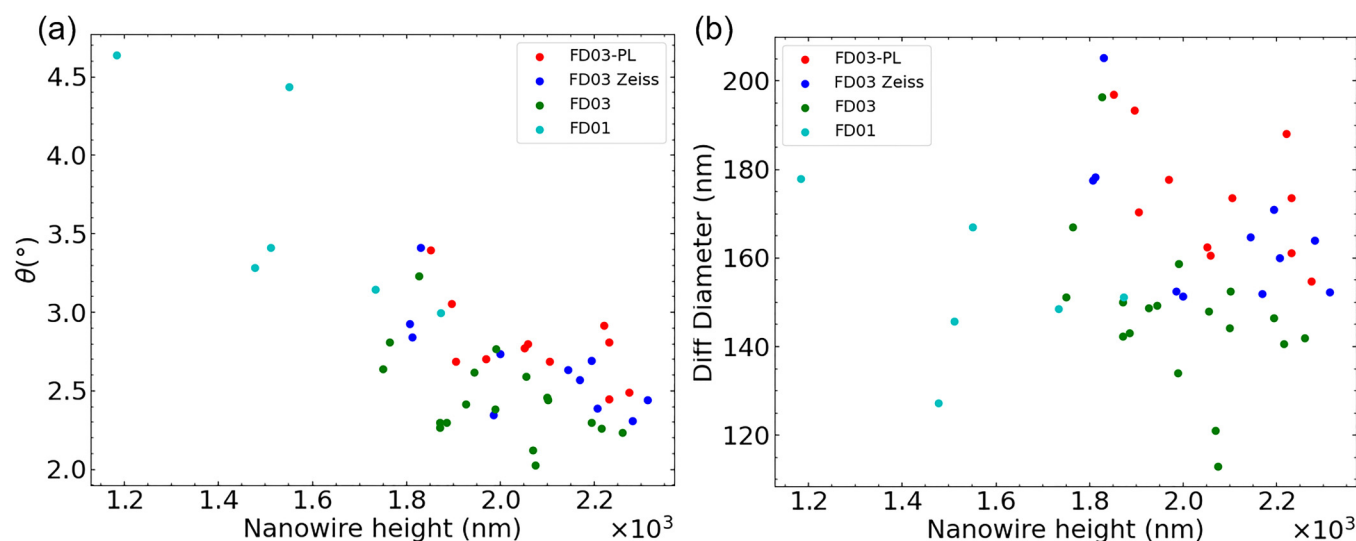


FIG. 5. (a) Relation between the etch depth and the tapering angle for different samples of wafers FD01, FD03, and FD03-PL. The details of these samples are provided in the [supplementary material](#). (b) Difference between the top and the bottom diameters of the etched nanowires vs the etch depth for different samples of wafers FD01, FD03, and FD03-PL.

same total etch time but with different resulting nanowire length. A better method to identify areas for improving the recipe is by studying the tapering angle for sets of nanowire samples with equal height.

To better understand the general trend, we examined groups of nanowire samples with a maximum nanowire height difference of 100 nm. It was observed that a longer etching cycle length of 60 s consistently results in a smaller tapering angle but compromises the tapering profile. An increasing CH_4/H_2 ratio leads to a decreasing tapering. Finally, longer descum cycle lengths increase the tapering angle.

A final investigation was carried out with respect to the temperature. The standard recipe was used to etch samples 1 and 2, while samples 3 and 4 were etched using the adjusted recipe (see Sec. 4 in the [supplementary material](#), Table FD05). Samples 1 and 3 were subjected to thermal isolation, whereas Fomblin oil was applied to the sample carrier within the Sentech ICP for samples 2 and 4. Nanowire arrays etched using the adjusted recipe exhibited a better tapering angle, even though their wire lengths were equal or shorter. The use of Fomblin oil also leads to a reduction in tapering. This may be due to the lower temperatures of the samples, which allow for more polymer formation on the surfaces, improving surface passivation and anisotropic etching. With lower temperatures, the chemical etching should slow down, particularly for the sidewalls, while re-deposition of etch products or sputtered material should increase. Sample 2 shows a less pronounced base-tapered profile compared to sample 1, supporting this explanation.

We have demonstrated that it is possible to attain a modest enhancement in both the tapering angle and the etched profile by using the adjusted etching recipe (Table I) with a higher methane/hydrogen ratio. Additionally, we have shown the importance of maintaining good thermal contact with the He-back-cooled sample

carrier through the application of Fomblin oil. This facilitates increased surface passivation, which further contributes to improving the overall outcome of the process. The best outcome achieved in terms of a low tapering angle for a nanowire, was a nanowire with a tapering angle of 1.8° , as shown in Fig. 6(a). Furthermore, this result provides insights into a route for achieving the optimum tapering angle of 1.2 – 1.3 degrees [see Fig. 1(c)] to obtain the optimum P_{esc} .¹⁰

V. MEASUREMENTS OF THE EXTERNAL RADIATIVE EFFICIENCY VS TAPERING ANGLE

We have experimentally verified the influence of the tapering angle on the external radiative efficiency, which is proportional to the integrated photoluminescence intensity, of an array of tapered InP nanowires on an InP substrate. We have shown in Fig. 1(c) that \bar{P}_{esc} for a dipole positioned in the bottom straight part of tapered nanowire first increases with increasing tapering angle toward 62% at a tapering angle of 1.2° and subsequently decreases down to 20% at a tapering angle of 4.5° . According to that calculation, the photon escape probability is 38% at a tapering angle of 2.4° . This tapering angle will be investigated in a nanowire solar cell below.

It should be noticed that experiments on the external radiative efficiency measure the product of the internal radiative efficiency and the photon escape probability, where the internal radiative efficiency might easily vary between different samples fabricated with different etching recipes. In order to exclude any difference between the material qualities, the measurements are performed on samples fabricated from the same MOVPE grown wafer, thus assuring that the internal efficiency of the bulk InP material is equal. An increased internal radiative efficiency could account for

16 December 2023 09:09:16

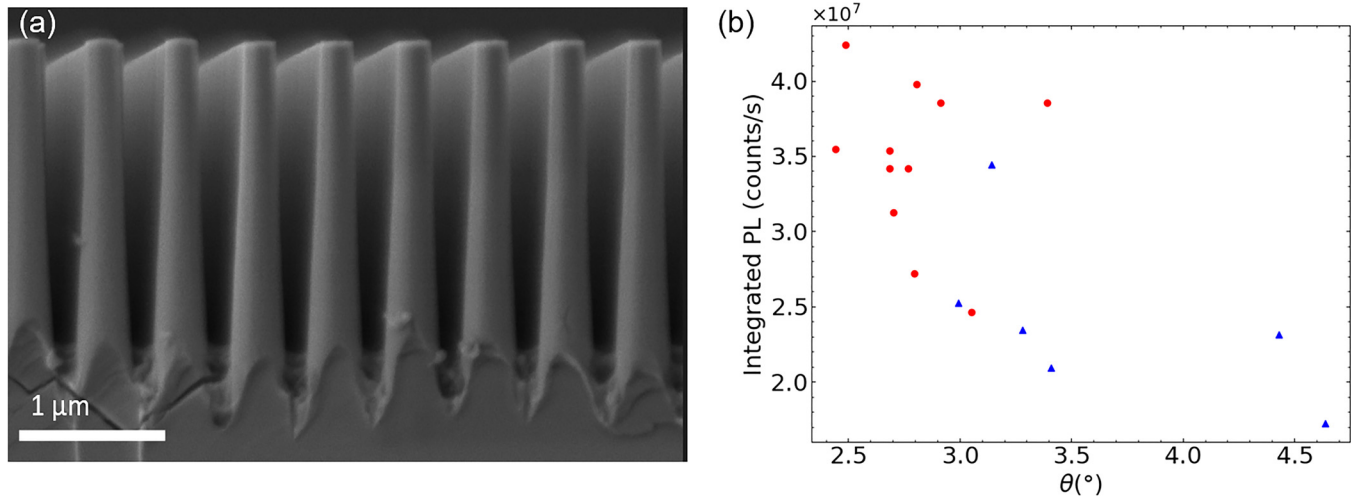


FIG. 6. (a) SEM image showing nanowires fabricated with the optimized etching recipe, reaching a tapering angle down to 1.8°. (b) Integrated photoluminescence intensity vs the tapering angle of our top-down etched undoped InP tapered nanowire arrays, showing a clear increase of the external radiative efficiency for small tapering angle. We plot the data for samples etched with different tapering angles of wafers FD03-PL (red bullets) and FD01 (blue triangles), details of which are described in the [supplementary material](#).

differences between samples, as different recipes might produce different surface roughness, influencing the surface recombination rate. In order to minimize the effects of different surface recombination for different tapering angles, all samples simultaneously underwent a digital etching procedure and were measured consecutively in order to minimize contamination or oxidization effects due to atmospheric exposure.

The results for the room temperature photoluminescence (PL) measurements for different undoped InP samples are shown in Sec. 5 in the [supplementary material](#), Fig. S2, where the PL intensity is plotted against the wavelength. As can be seen from that figure, the only significant difference between these undoped samples is the measured intensity. For this reason, the integrated PL will be used as a metric for the external radiative efficiency of the samples. The integrated PL is plotted against the tapering angle in Fig. 6(b). As can be seen from the figure, there is a trend for an increase of the integrated PL with a decreasing tapering angle, which indicates a higher external efficiency, either due to an increased internal efficiency or photon escape probability.

The difference in the apparent photoluminescent efficiency could also be caused by a difference in absorption efficiency. FDTD simulations of the light absorption in nanowire arrays, however, show that at least 80% of the solar light is absorbed in a nanowire with a length of 2 μm,¹¹ thus excluding that the large changes of the integrated PL intensity as observed in Fig. 6(b) are due to variations of the nanowire length. Since the calculated photon escape probability decreases from 38% at a tapering angle of 2.4°, down to 20% at a tapering angle of 4.5°,¹⁰ we argue that our simulated results are at least in qualitative agreement with the measured external radiative efficiencies as shown in Fig. 6(b), which also shows a decrease of the integrated PL with the same factor two as in the simulations.

VI. PROOF OF PRINCIPLE FOR AN INCREASED OPEN-CIRCUIT VOLTAGE AT REDUCED TAPERING

We have fabricated tapered InP nanowire solar cells using the design shown in Fig. 1(a). The details of the fabrication are given in Sec. 6 in the [supplementary material](#). In short, after MOVPE growth of the layer stack, tapered nanowires were etched with the standard recipe, yielding a tapering angle of 2.85° and a nanowire length of 1680 nm, which is referred to as sample SG01. A second sample was etched with an improved etching recipe, yielding a tapering angle of 2.46° and a nanowire length of 1780 nm, which is referred to as sample SG04. We subsequently performed three digital etching steps to remove surface damage stemming from the etching procedure and to reduce nonradiative surface recombination. The nanowires were passivated with a PO_x/Al₂O₃ stack deposited by atomic layer deposition, which has been shown to be effective for the passivation of undoped InP nanowires.²⁸ After planarization with benzocyclobutene (BCB), a 300 nm indium tin oxide (ITO) front contact was sputtered. For the back-contact, we first grow a strongly p-doped InGaAs layer at the back of the substrate and subsequently evaporate the Ti/Au metallization. After the ITO deposition, the solar cells are patterned in arrays of 6 × 6 cells as shown in Fig. 7(a). The cells were thermally annealed at 250 °C for 1 min both before patterning and after patterning to reduce the contact resistance between the ITO contact and the n-doped top part of the nanowires. We finally performed current-voltage measurements with a solar simulator that was calibrated with a GaAs reference solar cell.

We present the measured open-circuit voltages vs the short-circuit currents of both cell SG01 and SG04 in Fig. 7(b), where we have left out cells with unrealistically high J_{sc} since a few cells convert current from outside the cell area defined by the 500 × 500 μm² ITO front contacts. The best cells show solar cell

16 December 2023 09:09:16

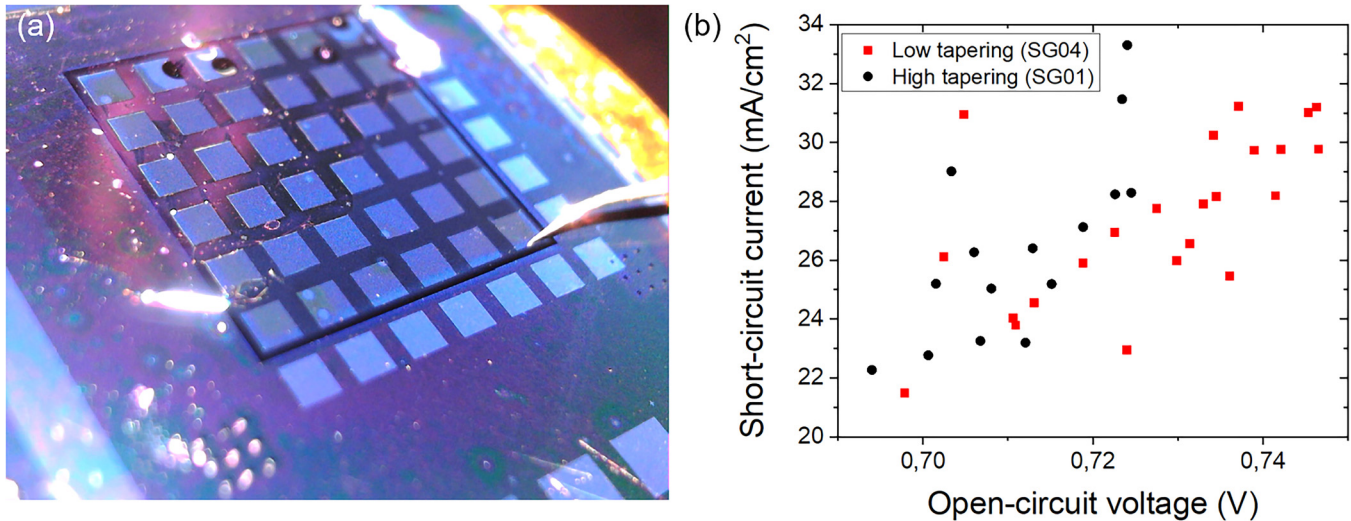


FIG. 7. (a) Image of the SG01 solar cells in the IV-measurement setup with a tungsten probe. (b) Comparison of the measured open-circuit voltages for the high tapering cell SG01 and the low tapering cell SG04.

performance comparable to our previous²⁹ record InP nanowire cell, but we also observe a considerable variation of the solar cell parameters between the different cells, which is most probably due to the ITO-nanowire contact, where not all nanowires are being electrically connected with the ITO front-contact layer. Most importantly, we observe a definite trend that the low tapering angle cells (SG04) tends to have a higher V_{oc} than the standard tapering cells (SG01). The SG01 cells have reasonably high V_{oc} between 694 and 724 mV and the SG04 cells have an increased V_{oc} between 697 and 746 mV. On the average, V_{oc} increased from 712 mV for SG01 toward 723 mV for SG04.

We subsequently try to understand the value of the measured open-circuit voltage by using Eq. (1). This equation, which directly results from thermodynamics, attributes the measured V_{oc} to the value of the external radiative efficiency $\eta_{ext}^{PL} = \eta_{int}^{PL} \bar{P}_{esc}$. It should be stressed that this equation neglects the influence of, e.g., imperfect solar light absorption, series resistances, and of nanowires that do not make an electrical contact to the ITO front contact. We first assume Eq. (1) to be valid and we use the value for $V_{oc}^{rad} = 1.037$ V from the literature.⁴ Using the measured V_{oc} of the best cells from samples SG01 and SG04, we arrive at values of the external radiative efficiency as presented in Table II.

TABLE II. Extracted external radiative efficiencies for our tapered nanowire solar cells.

Sample	Tapering angle	Nanowire height (nm)	Average measured V_{oc} (V)	η_{ext}^{PL}
SG01	2.85°	1680	0.712	3.45×10^{-6}
SG04	2.46°	1780	0.723	5.29×10^{-6}

We obtain a 53% higher external radiative efficiency η_{ext}^{PL} for the low tapering angle sample, while FDTD simulations shown in Fig. 1(c) yield a 17% increased \bar{P}_{esc} for a 2.46° tapering angle as compared to a 2.85° tapering angle nanowire. Given all the uncertainties involved in the fabrication process, which can easily affect the internal radiative efficiency, as well as the fact that the FDTD simulations were performed for a slightly different geometry (a single emitting dipole was positioned in a bottom straight part of the nanowire¹⁰), the agreement between the solar cell experiment and the simulations is encouraging.

The rather small nanowire height in our tapered nanowire solar cells results in a low solar light absorption probability. The effect of an imperfect solar light absorption in Eq. (1) is a reduction of the radiative limit V_{oc}^{rad} toward $V_{oc}^{max} = \frac{kT}{q} \ln\left(\frac{J_{sc}}{J_0}\right)$, where J_{sc} in the Shockley–Queisser (SQ) limit amounts to $J_{sc}^{SQ} = 33.7 \frac{mA}{cm^2}$ for InP at air mass 1.5 (AM1.5) conditions.³⁰ Using the known values for J_{sc}^{SQ} and V_{oc}^{rad} , we first calculate J_0 and subsequently calculate V_{oc}^{max} for different values of J_{sc} as shown in Table III.

We observe from Table III that a too short nanowire length is expected to reduce the solar light absorption and, thus, the value of J_{sc} , but this is hardly changing the open-circuit voltage V_{oc}^{max} in the

TABLE III. Variation of V_{oc}^{max} for a lossless cell with imperfect absorption as given by a reduced value of the short-circuit current.

J_{sc} (mA/cm²)	$V_{oc}^{max} = \frac{kT}{q} \ln\left(\frac{J_{sc}}{J_0}\right)$ (V)
33.7	1.037
32.3	1.0358
25	1.029

16 December 2023 09:09:16

radiative limit. We observe from Fig. 7(b) that the average J_{sc} only changes 1.4 mA/cm² between samples SG01 and SG04. We, thus, conclude from Table III that the influence of the nanowire length on the measured V_{oc} is quite small. A similar argument applies for nanowires which are not electrically connected to the ITO top contact. These wires will strongly reduce the J_{sc} , while not influencing the V_{oc} appreciably.

VII. CONCLUSIONS

We conclude that we are able to slightly increase the open-circuit voltage of our tapered nanowire solar cells by increasing the photon escape probability, which is achieved by reducing the nanowire tapering. The amount of V_{oc} -enhancement is larger than expected from theory assuming that the photon escape probability is the only factor affecting the measured V_{oc} , thus neglecting possible small variations in the internal radiative efficiency or the series resistance. In a broader perspective, this implies that increasing the photon escape probability, which is only 2% in a planar solar cell, provides an opportunity for a sizable increase of the open-circuit voltage in nanostructured solar cells. An enhancement of the V_{oc} beyond the value obtained in planar cells is most promising in tapered nanowire solar cells in which we predict that the photon escape probability can be increased up to 47.2% or 92% for normally tapered or inversely tapered nanowires, respectively.

SUPPLEMENTARY MATERIAL

See the supplementary material for details about (1) the radiative limit of a solar cell, (2) the rigorous coupled-wave analysis (RCWA), and (3) the particle swarm optimization. We also provide (4) the detailed etching parameters, (5) the photoluminescence spectra of tapered nanowire samples, and (6) details about the solar cell fabrication method.

ACKNOWLEDGMENTS

This work was supported by the Dutch Organization for Scientific Research NWO (Nos. TTW 15971 and 16PR1043) and Solumineus.

AUTHOR DECLARATIONS

Conflict of Interest

The authors have no conflicts to disclose.

Author Contributions

Emanuele Boichichio: Formal analysis (equal); Investigation (equal); Methodology (equal); Validation (equal); Writing – original draft (equal); Writing – review & editing (equal). **Ksenia Korzun:** Formal analysis (equal); Investigation (equal); Methodology (equal); Software (lead); Validation (equal); Writing – original draft (equal). **Friso Dubach:** Formal analysis (equal); Investigation (equal); Methodology (lead); Validation (equal); Writing – original draft (equal). **Bas T. van Gorkom:** Investigation (equal). **Roel J. Theeuwes:** Investigation (supporting). **Wilhelmus M. M. (Erwin) Kessels:** Supervision (supporting); Writing – review & editing

(supporting). **Jaime Gómez Rivas:** Conceptualization (equal); Funding acquisition (equal); Supervision (equal); Writing – review & editing (equal). **Jos E. M. Haverkort:** Conceptualization (equal); Funding acquisition (equal); Supervision (equal); Writing – review & editing (equal).

DATA AVAILABILITY

The data that support the findings of this study are available from the corresponding author upon reasonable request.

REFERENCES

- U. Rau, U. W. Paetzold, and T. Kirchartz, “Thermodynamics of light management in photovoltaic devices,” *Phys. Rev. B* **90**, 035211 (2014).
- U. Rau and T. Kirchartz, “On the thermodynamics of light trapping in solar cells,” *Nat. Mater.* **13**, 103–104 (2014).
- S. A. Mann *et al.*, “Quantifying losses and thermodynamic limits in nanophotonic solar cells,” *Nat. Nanotechnol.* **11**, 1071–1075 (2016).
- J. E. M. Haverkort, E. C. Garnett, and E. P. A. M. Bakkers, “Fundamentals of the nanowire solar cell: Optimization of the open circuit voltage,” *Appl. Phys. Rev.* **5**, 031106 (2018).
- W. Shockley and H. J. Queisser, “Detailed balance limit of efficiency of p-n junction solar cells,” *J. Appl. Phys.* **32**, 510–519 (1961).
- J. S. Van Der Burgt and E. C. Garnett, “Nanophotonic emission control for improved photovoltaic efficiency,” *ACS Photonics* **7**, 1589–1602 (2020).
- M. van Eerden, J. van Gastel, G. J. Bauhuis, E. Vlieg, and J. J. Schermer, “Comprehensive analysis of photon dynamics in thin-film GaAs solar cells with planar and textured rear mirrors,” *Sol. Energy Mater. Sol. Cells* **244**, 111708 (2022).
- M. A. Steiner *et al.*, “Optical enhancement of the open-circuit voltage in high quality GaAs solar cells,” *J. Appl. Phys.* **113**, 123109 (2013).
- T. Kirchartz, F. Staub, and U. Rau, “Impact of photon recycling on the open-circuit voltage of metal halide perovskite solar cells,” *ACS Energy Lett.* **1**, 731–739 (2016).
- K. Korzun, G. W. Castellanos, D. K. G. de Boer, J. Gómez Rivas, and J. E. M. Haverkort, “Nanowire solar cell above the radiative limit,” *Adv. Opt. Mater.* **9**, 1–7 (2021).
- N. Anttu *et al.*, “Absorption of light in InP nanowire arrays,” *Nano Res.* **7**, 816–823 (2014).
- S. L. Diedenhofen, O. T. A. Janssen, G. Grzelka, E. P. A. M. Bakkers, and J. Gómez Rivas, “Strong geometrical dependence of the absorption of light in arrays of semiconductor nanowires,” *ACS Nano* **5**, 2316–2323 (2011).
- B. Wang and P. W. Leu, “Enhanced absorption in silicon nanowire arrays for photovoltaics,” *Nanotechnology* **23**, 194003 (2012).
- O. T. A. Janssen, A. J. H. Wachtters, and H. P. Urbach, “Efficient optimization method for the light extraction from periodically modulated LEDs using reciprocity,” *Opt. Express* **18**, 24522–24535 (2010).
- R. J. Potton, “Reciprocity in optics,” *Rep. Prog. Phys.* **67**, 717–754 (2004).
- R. Carminati, J. J. Sáenz, J. J. Greffet, and M. Nieto-Vesperinas, “Reciprocity, unitarity, and time-reversal symmetry of the S matrix of fields containing evanescent components,” *Phys. Rev. A* **62**, 012712 (2000).
- N. Anttu, “Modifying the emission of light from a semiconductor nanowire array,” *J. Appl. Phys.* **120**, 043108 (2016).
- K. W. Robertson, R. R. LaPierre, and J. J. Krich, “Efficient wave optics modeling of nanowire solar cells using rigorous coupled-wave analysis,” *Opt. Express* **27**, A133 (2019).
- K. Nojiri, *Dry Etching Technology for Semiconductors* (Springer, Cham, 2012).
- T. Kim and J. Lee, “Optimization of deep reactive ion etching for microscale silicon hole arrays with high aspect ratio,” *Micro Nano Syst. Lett.* **10**, 12 (2022).

- ²¹K. T. Fountaine, W. H. Cheng, C. R. Bukowsky, and H. A. Atwater, "Near-unity unselective absorption in sparse InP nanowire arrays," *ACS Photonics* **3**, 1826–1832 (2016).
- ²²Y. J. Hung, S. L. Lee, B. J. Thibeault, and L. A. Coldren, "Fabrication of highly ordered silicon nanowire arrays with controllable sidewall profiles for achieving low-surface reflection," *IEEE J. Sel. Top. Quantum Electron.* **17**, 869–877 (2011).
- ²³F. Karouta, "A practical approach to reactive ion etching," *J. Phys. D: Appl. Phys.* **47**, 233501 (2014).
- ²⁴Y. Feuprier, "Influence of the gas mixture on the reactive ion etching of InP in CH₄–H₂ plasmas," *J. Vac. Sci. Technol. B* **15**, 1733 (1997).
- ²⁵T. R. Hayes, "Reactive ion etching of InP using CH₄/H₂ mixtures: Mechanisms of etching and anisotropy," *J. Vac. Sci. Technol. B* **7**, 1130 (1989).
- ²⁶M. A. Blauw, T. Zijlstra, and E. van der Drift, "Balancing the etching and passivation in time-multiplexed deep dry etching of silicon," *J. Vac. Sci. Technol. B* **19**, 2930 (2001).
- ²⁷B. Abraham-Shrauner, "Plasma etch profiles of passivated open-area trenches," *J. Vac. Sci. Technol. B* **19**, 711 (2001).
- ²⁸L. E. Black *et al.*, "Effective surface passivation of InP nanowires by atomic-layer-deposited Al₂O₃ with PO_x interlayer," *Nano Lett.* **17**, 6287–6294 (2017).
- ²⁹D. Van Dam *et al.*, "High-efficiency nanowire solar cells with omnidirectionally enhanced absorption due to self-aligned indium–tin–oxide Mie scatterers," *ACS Nano* **10**, 11414–11419 (2016).
- ³⁰S. Rühle, "Tabulated values of the Shockley-Queisser limit for single junction solar cells," *Sol. Energy* **130**, 139–147 (2016).